

Crystallographic and magnetic properties of Fe-doped SnO₂ nanopowders obtained by a sol–gel method

J. J. Beltran · L. C. Sánchez · J. Osorio · L. Tirado ·
E. M. Baggio-Saitovitch · C. A. Barrero

Received: 26 November 2009 / Accepted: 29 March 2010 / Published online: 10 April 2010
© Springer Science+Business Media, LLC 2010

Abstract We prepared Sn_{1-x}Fe_xO₂ ($x = 0, 0.03, 0.05, 0.10$, and 1.0) nanoparticles by the polymeric precursor method based on the modified Pechini process. Two types of starting reactants for both tin and iron were explored: Sn(II)/Fe(II) and Sn(IV)/Fe(III) precursors. Thermogravimetric analysis revealed that the precursor powders prepared from Sn(IV) have higher excess in ethylene glycol in comparison to precursor samples prepared from Sn(II). XRD patterns for those samples prepared from Sn(IV) and Fe(III) were adequately fitted by introducing only the cassiterite phase of SnO₂. Micro-Raman spectra also support these findings, and additionally it is found that the presence of iron broadened and reduced the intensities of the principal bands. ¹¹⁹Sn Mössbauer spectra indicated only the presence of Sn⁴⁺, whereas RT ⁵⁷Fe Mössbauer spectra suggested the presence of two Fe³⁺ sites located at different distorted sites. On the other hand, micro-Raman and ⁵⁷Mössbauer spectrometry showed the formation of hematite as impurity phase for those samples with iron

concentrations above ~ 5 at.%, prepared from Fe(II) and Sn(II) precursors. In addition, their XRD patterns revealed larger average grain sizes for the cassiterite phase of SnO₂ in comparison to those samples prepared from Sn(IV) and Fe(III).

Introduction

Tin oxide (SnO₂), normally known as cassiterite, is a typical wide band gap n-type semiconductor ($E_g = 3.6$ eV at 25°C) and one of the most widely used semiconductor oxides due to its chemical and mechanical stability [1, 2]. The cassiterite belongs to a rutile-type tetragonal system with a D_{14}^{4h} point group and with a $p4/mnm$ space group [3]. Tin oxide has many industrial applications such as catalytic support and gas sensors of toxic materials. It can be used as transparent electrode for solar cells, liquid crystal displays, anodes for lithium ion batteries and nano and ultrafiltration membranes [1, 2]. When doped with certain elements, SnO₂ exhibits a significant increase in the electrical conductivity [4, 5]. It has been found that Fe³⁺-doped SnO₂ nanoparticles have a higher catalytic activity and sensitivity to gases than undoped tin oxide [1]. However, maximum solubility of iron in tin oxide lattice remains imprecise [6–8]. In the last years, M-doped tin oxides (where M is a d-transition metal such as Fe, Co, Ni, Cr, Mn, etc. [7–13]) have been a subject of investigations due to their promising spintronics applications. Spintronic materials transport both charge and spin of free carriers in a controllable way [14]. One of the main features of these systems is that they can exhibit an intrinsic ferromagnetism at room temperature or above. This characteristic should not be related to the presence of hidden secondary phases or clusters associated with the

J. J. Beltran (✉) · L. C. Sánchez · J. Osorio · C. A. Barrero
Grupo de Estado Sólido, Instituto de Física, Universidad
de Antioquia, A.A. 1226, Medellín, Colombia
e-mail: jjbj08@gmail.com

J. J. Beltran
Instituto de Química, Universidad de Antioquia,
A.A. 1226, Medellín, Colombia

L. Tirado
Instituto de Física, Grupo de Optoelectrónica, Universidad
del Quindío, Armenia, Colombia

E. M. Baggio-Saitovitch
Centro Brasileiro de Pesquisas Físicas, Rio de Janeiro, Brazil

dopant. In these systems the foreign atoms must be homogeneously distributed at the cation sites in the host semiconductor crystalline structure [15]. It is well known that the synthesis method and the precursors employed in the preparation of Fe-doped SnO_2 nanoparticles can determine the physico-chemical, crystallographic, and magnetic properties of final product. In general, the preparations of pure and doped tin oxide have been carried out by different methods such as mechanical alloying, solid-state reaction method, and wet chemistry methods. The wet chemistry methods include co-precipitation, hydrothermal, solvothermal, sol-gel, among others [16–19]. The sol-gel method has several advantages over other methods such as its potential to produce high purity compounds with atomic scale homogeneity, significant reduction of the processing temperature and time required and high potential to control the particle size. The traditional sol-gel method utilized alkoxides as precursor, but this is relatively expensive and cannot be used at large scale. Another drawback of metal alkoxides is that they are moisture sensitive and need to be handled under a dry and inert atmosphere. The polymeric precursor method has been used during the last years as an alternative method to prepare ceramic oxides. By comparison with conventional sol-gel processing routes based on alkoxides, this technique requires cheaper precursors and allows the use of an aqueous system for the processing. The method was originally developed by Pechini [20]. The process involves the aqueous reaction of single or multiple metal ions with a poly functional acid such as citric acid (CA), to produce stable complexes and to prevent precipitation. These chelates undergo esterification, when heated with a poly-hydroxy alcohol, such as ethylene glycol (EG), to form a polymeric resin, subsequently establishing linkages between the chelates by a polyesterification reaction. The cations are expected to be dispersed uniformly throughout the polymeric resin. Additional heating of the resin in air allows the removal of the organic components and the formation of an amorphous dry product (powder precursor). The subsequent sinterization of the amorphous product at a suitable temperature leads to the formation of ceramic oxide. In the scientific and industrial ambits, it is of great importance to establish methodologies for obtaining pure samples, free from impurities and clustering of dopant ions for subsequent applications and to be sure that the material behavior is due to the properties generated by the dopant and not by the segregation of secondary phases. The principal aim of this article is to find proper ways of preparing Fe-doped SnO_2 nanoparticles by the polymeric precursor method based on the modified Pechini process by using two different tin and iron sources and studying their crystallographic and magnetic properties.

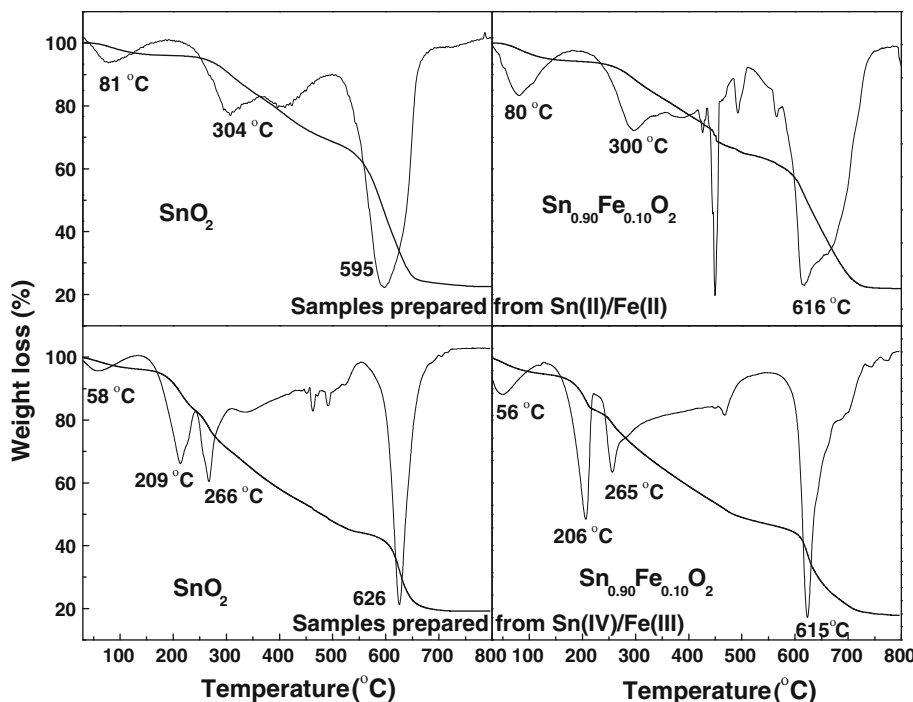
Experimental procedure

Samples of $\text{Sn}_{1-x}\text{Fe}_x\text{O}_2$ were obtained by the polymeric precursor method based on the modified Pechini process. The nominal compositions were $x = 0, 0.03, 0.05, 0.1$, and 1.0. Two different sources for both tin and iron were employed in the synthesis: $\text{SnCl}_2/\text{FeCl}_2 \cdot 4\text{H}_2\text{O}$ (Sn(II)/Fe(II)) and $\text{SnCl}_4 \cdot 5\text{H}_2\text{O}/\text{FeCl}_3 \cdot 6\text{H}_2\text{O}$ (Sn(IV)/Fe(III)). The different metal salts and the CA were separately dissolved in deionized water with a relation metal/CA of 1:3. According to the required composition for each tin chelate, the dopant was added dropwise under continuous magnetic stirring. Then EG in EG/CA ratio of 5 was added and the pH adjusted to 7.0 by adding NH_3 dropwise at 70 °C. Afterward, the beaker was kept on a hot plate at a temperature between 80 and 90 °C under constant stirring, to promote the polyesterification. The solution became more viscous and finally it gelled. This gel was then dried at 200 °C in air during 4 h to remove volatile components, resulting in a black solid mass, which is known as the precursor powder. This powder precursor was calcined at 600 °C for 1 h (heating rate: 5 °C/min) in air atmosphere. The thermal decomposition of the precursor powders were studied by thermogravimetric analysis (TG) using a TA Instruments Model Q 500. The stoichiometric mole ratio of elements for some samples was determined by X-ray fluorescence (XRF), using a Thermo Scientific WDRX spectrometer ARL OPTIM'X. Elemental analysis and mapping was carried out in a scanning electronic microscopy with energy dispersive X-ray analysis (EDAX), JEOL JSM 6490. The samples were investigated by XRD in a Bruker D8 Advance with a $\text{Cu K}\alpha$ source, in Bragg-Brentano geometry. The data were collected in the range 20°–80° in 2θ and the patterns were fitted using a program called MAUD [21], which combines the Rietveld method and a Fourier transform analysis. Micro-Raman measurements were performed on a Horiba Jobin-Yvon LabRam HR system. Raman scattering was excited with the 633 nm line of a He-Ne laser. The ^{119}Sn and ^{57}Fe Mössbauer spectra were recorded in a conventional Mössbauer spectrometer working in constant acceleration at room temperature. $\text{Ba}^{119}\text{SnO}_3$ and ^{57}Co sources were, respectively, utilized in the measurements. The ^{119}Sn Mössbauer spectra calibration velocity was performed by α -Fe and isomer shift ($\delta = 0$) of BaSnO_3 . The ^{57}Fe Mössbauer spectra were calibrated using α -Fe as standard absorber. The spectra were analyzed using the NORMOS program.

Results and discussion

Figure 1 shows the TG/DTG curves of pure SnO_2 and 10 at.% Fe-doped SnO_2 precursor powders obtained from

Fig. 1 TG/DTG curves of undoped SnO_2 and Fe-doped SnO_2 at 10% prepared from Sn(II)/Fe(II) (upper part) and Sn(IV)/Fe(III) (lower part)



both starting reactants: Sn(II)/Fe(II), upper part, and Sn(IV)/Fe(III), lower part. The thermal decomposition process for the samples prepared from Sn(II) is very complex, but it can be divided into three main regions of weight loss. The first stage (<200 °C) can be attributed to the removal of absorbed or superficial water molecules. In the second stage (200–500 °C) starts the decomposition of the amorphous product. The weight loss in this stage could be ascribed to the thermal degradation of the polyester chains, the thermal degradation of intermediate species formed during the gelation process (polymer chains formed from EG and CA) and to the elimination of the excess of EG and CA among the polyester macromolecular network [22–24]. In this temperature range the elimination of NH_4Cl is also possible (which could be condensed during the gelation process) [25, 26]. This observation is supported by the fact that the peaks of chloride ions were not observed by EDAX (not shown here). The third and last stage of weight loss (500–800 °C) is presumably due to the degradation of polymeric chelate chains through a process of combustion/oxidation. In this stage the formation and the crystallization of corresponding metal oxides took place. In the Fe-doped SnO_2 samples prepared from Sn(II)/Fe(II), the TG band corresponding to the last stage is broader in comparison to the undoped SnO_2 sample prepared with the same precursor. This behavior can be related to the presence of remnant chloride ions [27]. In Fig. 1 is also observed that the decomposition temperature of the polymeric chelate is higher in the Fe-doped SnO_2 than in the pure SnO_2 . This difference could be attributed to the

presence of Fe^{3+} ions, which can form more integrated polymeric chelates chains, therefore retarding the decomposition temperature. On the other hand, in the thermograms of undoped and Fe-doped SnO_2 samples prepared from Sn(IV)/Fe(III), the TG peak around 209 °C is probably due to the volatilization of EG. By comparison of the TG curves from both precursors, we can notice that in the samples prepared from Sn(IV) there are more residual EG (confirmed by the peak at 209 °C) and higher degradation of organic component (corroborated by the greater weight loss) in the second stage. In general, in the samples prepared from Sn(IV), the thermal decomposition temperature of polymeric chelate occurs at higher temperatures than those prepared from Sn(II), indicating a better complexation of the Sn^{4+} ions than the Sn^{2+} ones.

In studies EDAX for some $\text{Sn}_{1-x}\text{Fe}_x\text{O}_2$ samples, three different points were chosen randomly and about the same iron concentration was observed for all of them, suggesting homogeneous iron distribution. These results are in good agreement with other reports on similar samples [8]. In fact, the sol-gel chemical method has been reported to provide a uniform distribution of the dopant in the host system at low temperatures [8]. XRF for those samples with $x = 0.1$ prepared from Sn(II)/Fe(II) and Sn(IV)/Fe(III) showed values of about 0.073 and 0.101, respectively, in reasonable agreement with their nominal compositions.

The diffraction patterns of $\text{Sn}_{1-x}\text{Fe}_x\text{O}_2$ ($x = 0, 0.03, 0.05, 0.10$, and 1) nanoparticles prepared from Sn(II) are shown in Fig. 2. Notice that $x = 0$ is for pure SnO_2 , and $x = 1$ is for the so-called Fe(II) target. The diffraction

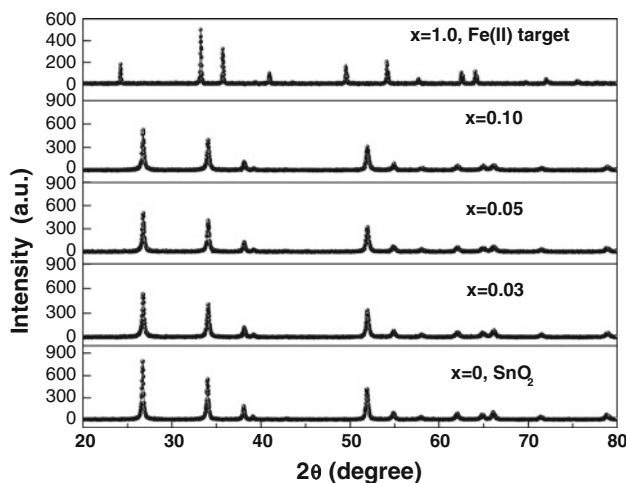


Fig. 2 XRD patterns of $\text{Sn}_{1-x}\text{Fe}_x\text{O}_2$ samples prepared from Sn(II) and Fe(II). *Solid spheres* are experimental data, whereas *solid lines* represent the fit using the Rietveld method

pattern of pure SnO_2 was fitted by introducing only the cassiterite phase. Peaks belonging to other phases such as romarchite (SnO) or metastable orthorhombic phase of SnO_2 were not detected [28, 29]. The pattern of Fe(II) target displays well defined peaks characteristic of hematite ($\alpha\text{-Fe}_2\text{O}_3$) [30]. The XRD patterns of $\text{Sn}_{1-x}\text{Fe}_x\text{O}_2$ samples did not clearly show the presence of hematite. The Fe doping in SnO_2 broadens symmetrically and reduces the intensity of all XRD peaks, pointing to a reduction in the average crystallite sizes with the Fe doping (see Fig. 3).

Figure 4 shows the XRD patterns of pure SnO_2 and Fe-doped SnO_2 samples prepared from Sn(IV) and Fe(III). All Bragg peaks were sharp at the top but wide at the tails,

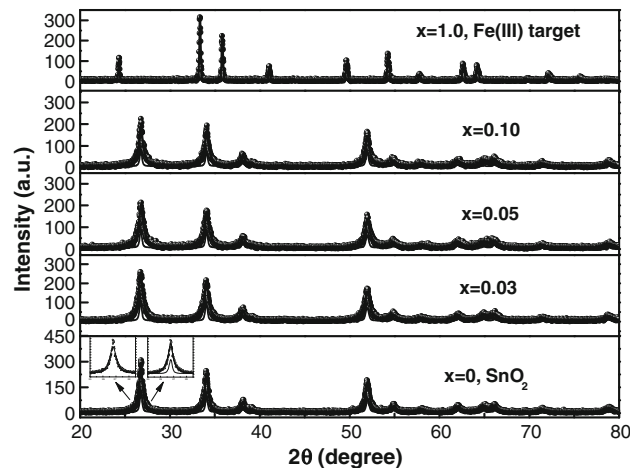


Fig. 4 XRD patterns of $\text{Sn}_{1-x}\text{Fe}_x\text{O}_2$ samples prepared from Sn(IV) and Fe(III). *Solid spheres* are experimental data, whereas *solid lines* represent the fit using the Rietveld method. The insets show a selected Bragg peak fitted with one (left part) or two (right part) components

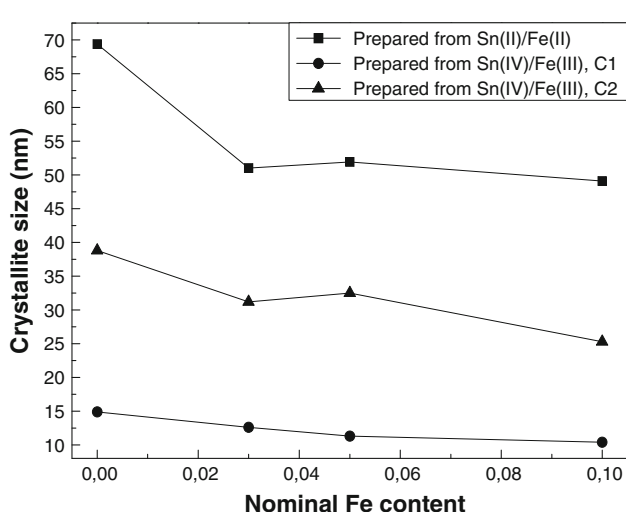


Fig. 3 Average crystallite sizes versus nominal Fe content for $\text{Sn}_{1-x}\text{Fe}_x\text{O}_2$ samples from both precursors. C1 and C2 are components 1 and 2 used to fit the XRD patterns of those samples prepared from Sn(IV)/Fe(III) precursors

suggesting the presence of two SnO_2 components. In fact, the fitting of the XRD patterns improved by introducing two cassiterite phases instead of one (see the inset in Fig. 4). According to Martinelly and Ferretti [31], these components can be attributed to two rutile-type phases (Sn-enriched and Sn-depleted). These components may have another different origin, one component (C1) due to the presence of SnO_2 with small average grain sizes and another component (C2) with larger sizes. The C1 proportion was larger than C2 for all samples. In the diffractograms of $\text{Sn}_{1-x}\text{Fe}_x\text{O}_2$ samples, the hematite peaks were not detected and the incorporated Fe has a similar effect as in the samples prepared from Sn(II). In these samples the Bragg peaks were more broadened and less intense compared with the ones from Sn(II), indicating minor crystallinity for those SnO_2 samples prepared from Sn(IV). These results indicate that the precursors' nature has significant influence in the final properties of the oxide. Figure 3 shows the variation of the average crystallite size with nominal Fe content for both precursors. It is clear that the addition of Fe, in both cases, prevents the growing of SnO_2 crystallites, and that for a given iron content, the average grain sizes for those samples prepared from Sn(II)/Fe(II) were larger than for those prepared from Sn(IV)/Fe(III). The difference in the average crystallite sizes, could be attributed to the higher excess in EG between the polymeric chains for the samples prepared from Sn(IV) in comparison to those from Sn(II). The combustion heat generated during the burn out of EG would facilitate early thermal decomposition of the polyester network, and this probably could make that the polyester chains prepared from Sn(IV) arrived at decomposition's final stage in less amount than those from Sn(II). The higher combustion

heat, generated by greater temperature and shorter polymeric chains, likely increase the velocity of exothermic process. The opposite can occur in those samples prepared from Sn(II), where this process could be slower and possibly increase the formation of agglomerates. Similar results were reported by Qiu and coworkers in synthetic PZT 95/5, for which the EG among the polymeric network promote the thermal decomposition of the polyesters and result in the formation of small crystalline size particles [24].

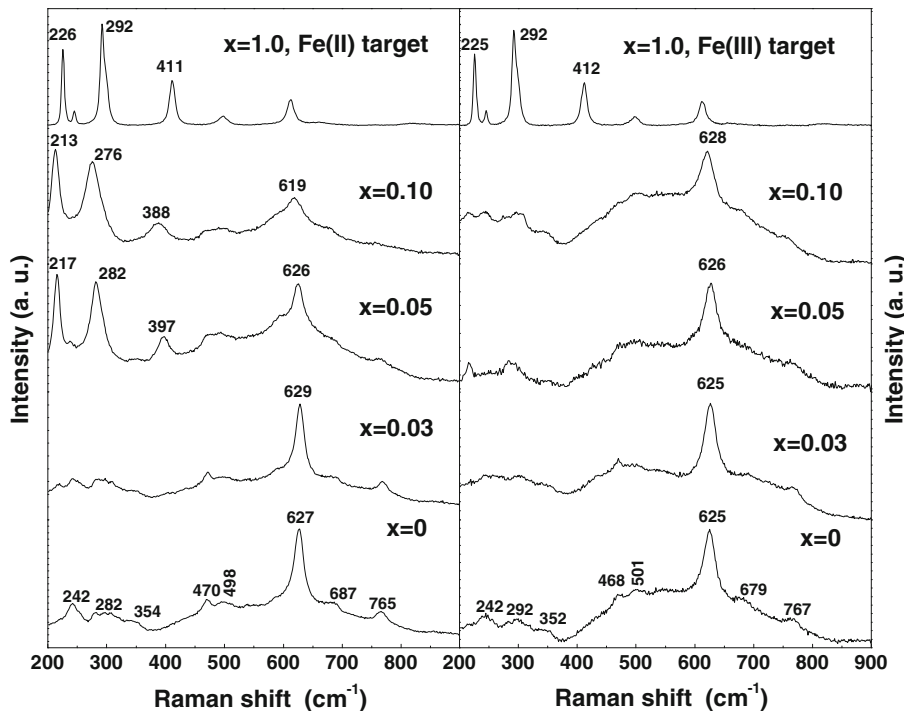
The peaks of the micro-Raman spectrum of SnO_2 can be divided into two groups. One of them belonging to microcrystalline and crystalline SnO_2 phases, or modes from the bulk, and another group, corresponding to surface phononic and acoustical modes. These last modes dominate when the crystallite size is small enough and are only observed in nanometer-sized SnO_2 grains. The vibrations modes from the second group can result from an intrinsic local disorder or vacant sites in the oxide structure [32, 33]. The normal modes of vibrations at the Brillouin zone of SnO_2 are given by [34]:

$$\Gamma_{\text{rutile}} = 1\text{A}_{1g} + 1\text{A}_{2g} + 1\text{A}_{2u} + 1\text{B}_{1g} + 1\text{B}_{2g} + 2\text{B}_{1u} \\ + 1\text{E}_g + 3\text{E}_u$$

Of these modes, two are IR active (the single A_{2u} and the triply degenerated E_u mode), four modes are Raman active (three non-degenerate modes, A_{1g} , B_{1g} , B_{2g} and the doubly degenerate E_g) and two are silent (A_{2g} and B_{1u}). One A_{2u} and two E_u modes are acoustic and have transverse (TO) and longitudinal optical (LO) vibrations [3, 34]. Figure 5

shows the micro-Raman spectra of pure SnO_2 and Fe-doped SnO_2 samples obtained from Sn(II), left part and from Sn(IV), right part. The micro-Raman spectrum of pure SnO_2 exhibits peaks corresponding to the first group located at about 627, 470, and 765 cm^{-1} . These peaks are attributed to the A_{1g} , E_g , and B_{2g} vibrational modes, which are in agreement with those reported for a rutile SnO_2 single crystal [35]. The peaks located at 687, 498, 354, 242, and 282 cm^{-1} are related to A_{2u} (ν_{LO}), A_{2u} (ν_{TO}), E_u ($\nu_{2\text{LO}}$), E_u (ν_{TO}), and E_u (ν_{LO}) vibrational modes, respectively, corresponding to second group [34, 35]. The Fe(II) target exhibited Raman characteristic peaks of hematite at around 226 and 498 cm^{-1} , which can be assigned to the A_{1g} modes [36], as well as 245, 290, 407, and 609 cm^{-1} , and which are related to the E_g modes. The micro-Raman spectrum of the $\text{Sn}_{0.97}\text{Fe}_{0.03}\text{O}_2$ sample does not show peaks associated with hematite and the vibrational modes of SnO_2 were shifted to higher frequencies, indicating microstructural changes. The micro-Raman spectrum of $\text{Sn}_{0.95}\text{Fe}_{0.05}\text{O}_2$ sample shows peaks corresponding to hematite, which are shifted to higher wavelength numbers and also displays residual SnO_2 peaks. By increasing the iron concentration to 10 at.%, the peaks of the iron phase shifted to higher wavelength numbers and become broader. These results suggest that the solubility of iron in SnO_2 for those samples prepared from Sn(II) and Fe(II) is lower to 5 at.%. Above this value, hematite, most likely, Sn-doped hematite, starts to be formed. For our samples, micro-Raman spectroscopy has demonstrated a higher sensibility to the presence of minor amounts of hematite impurities in

Fig. 5 Micro-Raman spectra for $\text{Sn}_{1-x}\text{Fe}_x\text{O}_2$ (0, 0.03, 0.05, 0.1, and 1.0) powders prepared from Sn(II)/Fe(II) (left part) and Sn(IV)/Fe(III) (right part)



comparison to XRD. On the other hand, the micro-Raman spectrum of pure SnO_2 prepared from Sn(IV) exhibited similar vibrational modes as the spectrum of the pure SnO_2 sample synthesized from Sn(II), but the peaks were more broadened and less intense. These observations could be related with a lower crystallinities and smaller average grain sizes of samples prepared from Sn(IV) in comparison to those samples prepared from Sn(II) (in agreement with the results found by XRD). As shown in Fig. 5, in the Fe-doped samples ($x = 0.03, 0.05$, and 0.10) prepared from Sn(IV), the peaks of hematite were not detected. These observations, together with the XRD results, indicate the formation of a $\text{Sn}_{1-x}\text{Fe}_x\text{O}_2$ solid solution, where Sn^{4+} substitutes by Fe^{3+} ions. Therefore, the iron solubility in SnO_2 samples from Sn(IV) and Fe(III) is higher than about 10 at.%. These results indicate that the precursors' nature is an important parameter to synthesize solid solutions of $\text{Sn}_{1-x}\text{Fe}_x\text{O}_2$ by this method.

The ^{119}Sn Mössbauer spectra of the undoped and Fe-doped SnO_2 samples prepared from both precursors are shown in Fig. 6 and the derived hyperfine parameters are shown in Table 1. All samples were fitted with only one component, which consists of one broad and symmetric doublet. The results indicate that there is no tin valence else than Sn^{4+} in all the samples. The non-zero quadrupole splittings and broad lines could be attributed to the presence of structural defects, like oxygen vacancies around Sn^{4+} [37], or intrinsic local disorder of SnO_2 . The hyperfine parameters of the 3 at.% Fe-doped SnO_2 sample prepared from Sn(II) increase in comparison with those values for the pure SnO_2 sample. These results suggest higher oxygen vacancies and structural disorder created by the

Table 1 ^{119}Sn Mössbauer parameters for undoped and Fe-doped SnO_2 samples prepared from both precursors

Sample	δ (mm/s)	Δ (mm/s)	Γ (mm/s)
Samples prepared from Sn(II)/Fe(II)			
SnO_2	0.00	0.50	1.13
$\text{Sn}_{0.97}\text{Fe}_{0.03}\text{O}_2$	0.00	0.77	1.76
$\text{Sn}_{0.95}\text{Fe}_{0.05}\text{O}_2$	0.01	0.68	1.54
$\text{Sn}_{0.90}\text{Fe}_{0.10}\text{O}_2$	0.01	0.57	1.58
Samples prepared from Sn(IV)/Fe(III)			
SnO_2	0.00	0.47	1.36
$\text{Sn}_{0.97}\text{Fe}_{0.03}\text{O}_2$	0.00	0.48	1.65
$\text{Sn}_{0.95}\text{Fe}_{0.05}\text{O}_2$	0.00	0.65	1.76
$\text{Sn}_{0.90}\text{Fe}_{0.10}\text{O}_2$	0.00	0.70	1.86

Estimated errors are of about ± 0.01 mm/s for the isomer shift, δ the quadrupole splitting, Δ , and the linewidth, Γ

dopant. A systematic reduction in the quadrupole splittings are observed for both 5 and 10 at.% Fe-doped SnO_2 samples. According to micro-Raman results this tendency can be explained as a possible segregation of a portion the iron atoms from the Fe-doped SnO_2 structure to form a secondary phase as described above. The segregation of hematite could produce a diminution in the oxygen vacancies around Sn(IV) in comparison with the 3 at.% Fe-doped SnO_2 sample. In the Fe-doped SnO_2 samples prepared from Sn(IV), the linewidths and the quadrupole splittings increase with increasing Fe doping (see Table 1). These results indicate that the increment of the iron content creates more oxygen vacancies and defects close to the Sn^{4+} .

Fig. 6 Room temperature ^{119}Sn Mössbauer spectra of $\text{Sn}_{1-x}\text{Fe}_x\text{O}_2$ samples prepared from Sn(II)/Fe(II) (left part) and Sn(IV)/Fe(III) (right part)

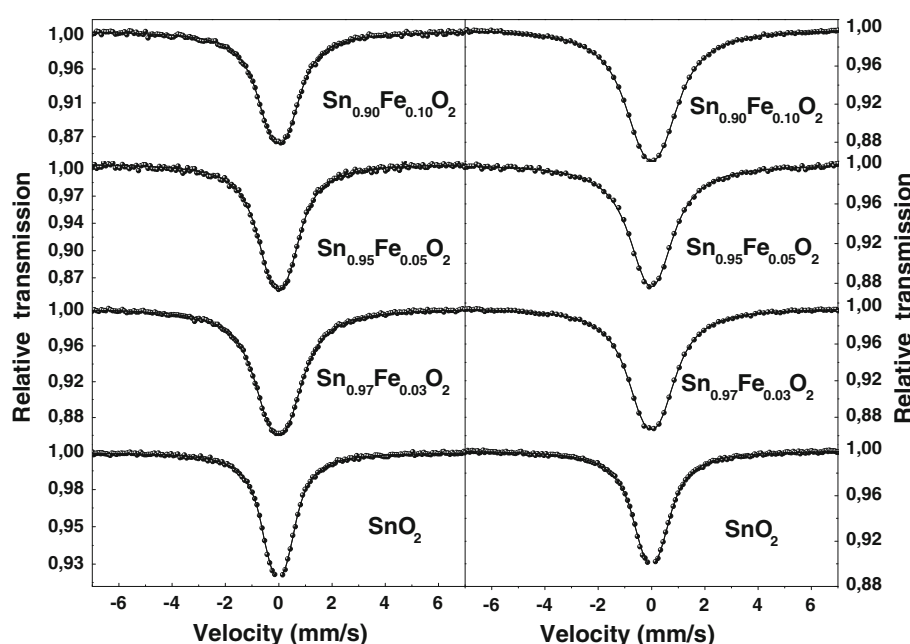


Fig. 7 Room temperature ^{57}Fe Mössbauer spectra of $\text{Sn}_{1-x}\text{Fe}_x\text{O}_2$ samples prepared from Sn(II)/Fe(II) along with the spectrum of Fe(II) target

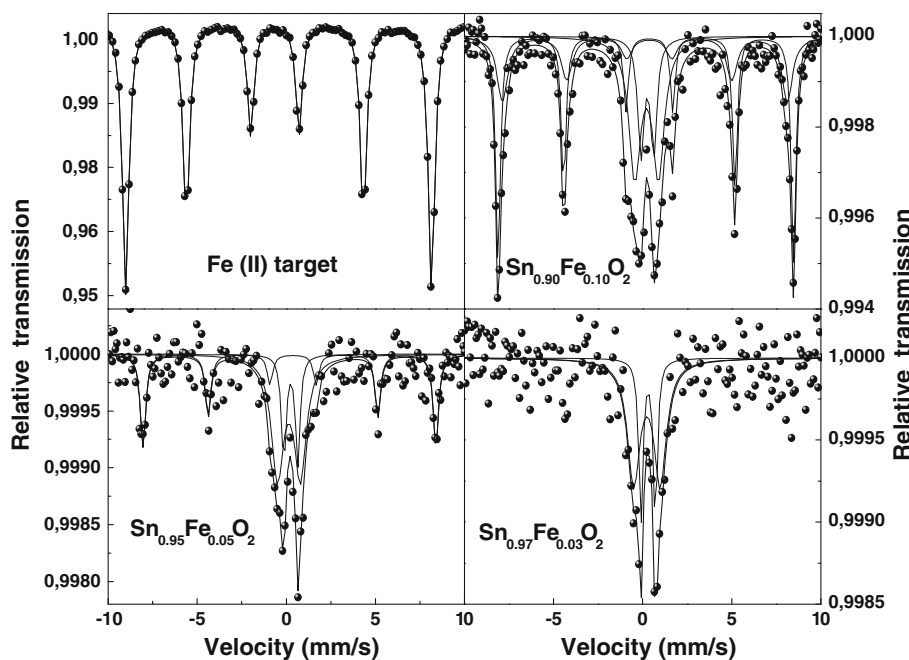


Table 2 ^{57}Fe Mössbauer parameters of Fe-doped SnO_2 samples prepared from Sn(II)/Fe(II)

Sample	Component	δ (mm/s)	2ε or Δ (mm/s)	$\langle B \rangle$ (T)	Γ (mm/s)	A (%)
Target Fe(II)	Sextet	0.37	-0.20	51.7	0.41	100
$\text{Sn}_{0.97}\text{Fe}_{0.03}\text{O}_2$	D1	0.41	0.81		0.28	31
	D2	0.35	1.49		0.83	69
$\text{Sn}_{0.95}\text{Fe}_{0.05}\text{O}_2$	S1	0.39	-0.24	51.0	0.38	65
	D1	0.36	0.79		0.27	14
	D2	0.27	1.26		0.85	51
$\text{Sn}_{0.90}\text{Fe}_{0.10}\text{O}_2$	S1	0.38	-0.20	51.6	0.33	37
	S2	0.36	-0.25	49.6	0.63	24
	D1	0.37	0.71		0.43	12
	D2	0.33	1.33		0.79	27

Estimated errors are of about ± 0.01 mm/s for the isomer shift, δ , the quadrupole splitting, Δ , the quadrupole shift, 2ε , and the linewidth, Γ , of about ± 0.1 T for the average magnetic hyperfine field, B , and of about $\pm 2\%$ for the relative area, A . D1, D2, S1, and S2 are doublet 1, doublet 2, sextet 1, and sextet 2, respectively

Figure 7 shows the ^{57}Fe Mössbauer spectra of $\text{Sn}_{1-x}\text{Fe}_x\text{O}_2$ ($x = 0.03, 0.5, 0.10$, and 1.0) samples prepared from Sn(II)/Fe(II) and the derived hyperfine parameter are shown in Table 2. The spectrum of Fe(II) target displays a well defined sextet with hyperfine parameters belonging to hematite [38]. The paramagnetic signal of the doped samples was properly fitted with two doublets, whose hyperfine parameters, suggest that the Fe ions are in high spin $3+$ states, in an octahedral environment. No evidence of any Fe^{2+} ions was detected in these samples. The introduction of a second doublet improves considerably, both visual and statistically, the fitting. These two components suggest that there are two kinds of iron sites in different chemistry environments. Doublet D1 is assigned to Fe^{3+} ions replacing Sn^{4+} ions in a less distorted and/or

less defective sites, whereas doublet D2 comes from the iron also replacing tin ions close to more defective sites [8]. For the 3 at.% Fe-doped sample, hematite was not detected, whereas for both 5 and 10 at.% Fe-doped samples its presence was clearly evidenced. The better fitting of $\text{Sn}_{0.95}\text{Fe}_{0.05}\text{O}_2$ sample was achieved with only one magnetic component. The hyperfine parameters (see Table 2) suggested the formation of distorted hematite probably doped with Sn^{4+} , as observed in a previous work [39]. On the other hand, the 10 at.% Fe-doped SnO_2 sample was adequately fitted with two magnetic components. The hyperfine parameters of sextet 1 (S1) with higher magnetic hyperfine field is attributed to crystalline hematite, whereas sextet 2 (S2) with lower magnetic hyperfine field could be due to Sn^{4+} -doped hematite [40]. The results obtained by

Fig. 8 Room temperature ^{57}Fe Mössbauer spectra of $\text{Sn}_{1-x}\text{Fe}_x\text{O}_2$ samples prepared from Sn(IV)/Fe(III) along with the spectrum of Fe(III) target

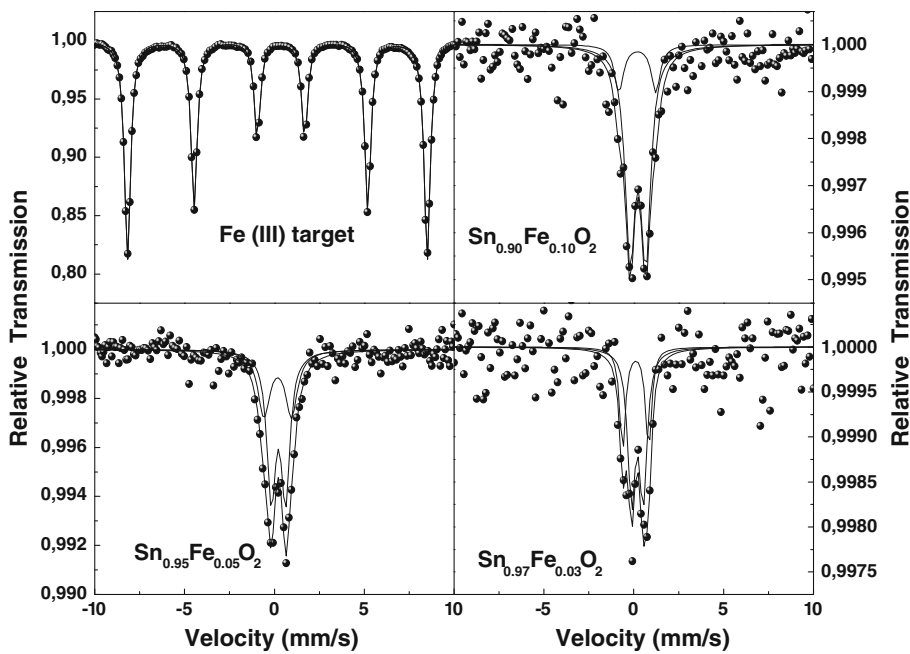


Table 3 ^{57}Fe Mössbauer parameters of Fe-doped SnO_2 samples prepared from Sn(IV)/Fe(III)

Sample	Component	δ (mm/s)	2ε or Δ (mm/s)	$\langle B \rangle$ (T)	Γ (mm/s)	A (%)
Target Fe(III)	Sextet	0.37	-0.20	51.7	0.41	100
$\text{Sn}_{0.97}\text{Fe}_{0.03}\text{O}_2$	D1	0.31	0.65		0.39	64
	D2	0.21	1.44		0.71	36
$\text{Sn}_{0.95}\text{Fe}_{0.05}\text{O}_2$	D1	0.33	0.79		0.57	61
	D2	0.29	1.53		0.81	39
$\text{Sn}_{0.90}\text{Fe}_{0.10}\text{O}_2$	D1	0.35	0.88		0.66	82
	D2	0.31	2.06		0.86	18

Estimated errors are of about ± 0.01 mm/s for the isomer shift, δ , the quadrupole splitting, Δ , the quadrupole shift, 2ε , and linewidth, Γ , estimated errors are about ± 0.01 mm/s for the isomer shift, δ quadrupole splitting, Δ , and linewidth, Γ , of about ± 0.1 T for the average magnetic hyperfine field, B , and of about $\pm 2\%$ for the relative area, A . D1 and D2, are doublet 1 and doublet 2, respectively

^{57}Fe Mössbauer spectrometry are in agreement with micro-Raman results. By increasing the Fe dopant concentrations above 3 at.%, the solubility limit is overpassed and α -[$(\text{Fe}_{2-x}\text{Sn}_x)\text{O}_3$] forms as a secondary phase. The ^{57}Fe Mössbauer spectra of Fe-doped SnO_2 sample prepared from Sn(IV) and the Fe(III) target are shown in Fig. 8 and the derived hyperfine parameters are shown in Table 3. In the Mössbauer spectra of these samples neither hematite nor any another magnetic component were evidenced. Table 3 shows that the isomer shift, quadrupole splitting and linewidth increase for both doublets with increasing Fe content, suggesting a higher structural and local disorder, due to the Fe^{3+} incorporation into crystalline structure of SnO_2 . It is interesting to notice that for a given iron concentration the linewidth of the D1 component is always greater for those samples prepared from Sn(IV) than for those prepared from Sn(II). This observation is

related with more defects and/or less degree of crystallinity in the samples prepared from Sn(IV) than from Sn(II).

Figure 9 shows the magnetization, M , versus magnetic field, H , curve for the 10 at.% Fe-doped SnO_2 sample prepared from Sn(IV). As shown in the figure, this curve consists of a linear paramagnetic component and a magnetic hysteresis loop. The existence of coercivity field and the lack of saturation magnetization (maximum applied field was of 30 kOe) in the sample clearly rules out the presence of superparamagnetic particles of iron oxides [9]. These observations indicate that the sample is ferromagnetic at room temperature. Now, the Mössbauer spectrum for this sample does not show a sextet component at room temperature, therefore the Fe^{3+} ions are not responsible for the magnetic ordering. Thus, it seems that the defects in the sample can become magnetically ordered and may become

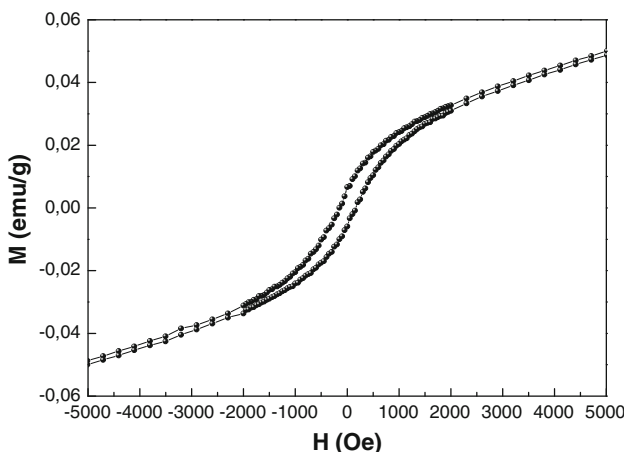


Fig. 9 Room temperature hysteresis loop of $\text{Sn}_{0.9}\text{Fe}_{0.10}\text{O}_2$ sample prepared from Sn(IV)/Fe(III)

the main source of ferromagnetism. Similar results were obtained by Nomura and coworkers [8].

Conclusions

We investigated the effects of iron concentration ($x = 0, 0.03, 0.05, 0.10$, and 1.0) and starting tin and iron reactants on the degree purity and the physical properties of $\text{Sn}_{1-x}\text{Fe}_x\text{O}_2$ nanoparticles prepared by the modified Pechini process. XRD patterns of all samples showed only peaks characteristic of cassiterite phase SnO_2 . Raman and ^{57}Fe Mössbauer spectra suggested that Fe-doped SnO_2 samples prepared from Sn(II) and Fe(II), with the exception of the 3 at.% Fe, showed the presence of hematite as an impurity phase, whereas all samples prepared from Sn(IV) and Fe(III) were impurity free. The samples prepared from Sn(II) precursors showed larger average grain sizes and higher degree of crystallinity than those prepared from Sn(IV). This behavior can be attributed to the higher excess in EG between the polymeric chains for the samples prepared from Sn(IV) in comparison to those from Sn(II). ^{119}Sn Mössbauer spectra revealed only the presence of Sn^{4+} . ^{57}Fe Mössbauer spectra suggested the presence of two Fe^{3+} ions located at different SnO_2 distorted sites. Doublet 1 with the lowest quadrupole splitting values were assigned to less distorted sites and doublet 2 with the largest quadrupole splitting values were assigned to more distorted sites. The 10 at.% Fe-doped SnO_2 prepared from Sn(IV) presented a linear paramagnetic and a magnetic hysteresis loop. This hysteresis loops indicate that this sample is ferromagnetic at room temperature, whose signal could not related with a long range magnetic iron ordering.

Acknowledgements CBPF-Centro Brasileiro de Pesquisas Físicas. Departamento de Física Experimental e Baixas Energias, CODI-

Universidad de Antioquia (Sustainability Program for the Solid State Research Group 2009–2010), CENM; Gobernación del Cesar by technical cooperation agreement No 0.38 2006 Colciencias-Universidad Popular del Cesar in association with the Universidad de Antioquia.

References

- Fang LM, Zu XT, Li ZJ, Zhuc S, Liu CM, Zhoue WL, Wang LM (2008) *J Alloys Compd* 454:261
- Zhang J, Gao L (2004) *J Solid State Chem* 177:1425
- Traylor JG, Smith HG, Nicklow RM, Wilkinson MK (1971) *Phys Rev B* 3:3457
- Ponce MA, Parra R, Castro MS, Aldao CM (2007) *J Mater Sci: Mater Electron* 18:1171
- Parra R, Ramajo LA, Góes MS, Varela JA, Castro MS (2008) *Mater Res Bull* 43:3202
- Melghit K, Bouziane K (2006) *Mater Sci Eng B* 128:58
- Das K, Adhikari R, Karmakar D, Chandrasekhar Rao TV, Ghtak J (2008) *Phys Rev B* 78:024404
- Nomura K, Barrero CA, Sakuma J, Takeda M (2007) *Phys Rev B* 75:184411
- Punnoose A, Hays J, Thurber A, Engelhard MH, Kukkadapu RK, Wang C, Shutthanandan V, Thevuthasan S (2005) *Phys Rev B* 72:054402
- Bouaine A, Brihi N, Schmerber G, Ulhaq-Bouillet C, Colis S, Dinia A (2007) *J Phys Chem C* 111:2924
- Archer P, Radovanovic PV, Heald SM, Gamelin DR (2005) *J Am Chem Soc* 127:14479
- Zuo Y, Ge S, Zhang L, Yan S, Zhou X, Xiao Y (2009) *J Alloys Compd* 475:60
- Xiao Y, Ge S, Xi L, Zuo Y, Zhou X, Zhang B, Zhang L, Li C, Han X, Wen Z (2008) *Appl Surf Sci* 254:7459
- Ohno H (1998) *Science* 281:951
- Das Sarma S, Hwang EH, Kaminski A (2003) *Solid State Commun* 127:99
- Wang S, Wang Y, Jiang J, Liu R, Li M, Wang Y, Su Y, Zhu B, Zhang S, Huang W, Wu S (2009) *Catal Commun* 10:640
- Firooz AA, Mahjoub AR, Khodadadi AA (2008) *Mater Lett* 62:1789
- Cheng G, Wu K, Zhao P, Cheng Y, He X, Huang K (2007) *J Cryst Growth* 309:53
- Ristic M, Ivanda M, Popovic S, Music S (2002) *J Non-Cryst Solids* 303:270
- Pechini MP (1967) US Patent 3,330,697, 11 July 1967
- Lutterotti L (2002) MAUD, Materials analysis using diffraction, version: 1.84. <http://www.ing.unitn.it/~maud/>
- Mathur S, Shen H (2002) *J Sol-Gel Sci Technol* 25:147
- Zhang C, Shen X, Zhou J, Ping M, Cao K (2007) *J Sol-Gel Sci Technol* 42:95
- Qiu S, Fan H, Zheng X (2007) *J Sol-Gel Sci Technol* 42:21
- Razpotnik T, Francetić V, Macek J (2006) *Mater Technol* 40:69
- Sangaletti L, Depero LE, Allieri B, Pioselli F, Angelucci R, Poggi A, Tagliani A, Nicoletti S (1999) *J Eur Ceram Soc* 19:2073
- Fraiggi L, Lamas D, Walsöe de Reca N (2001) *Mater Lett* 47:262
- Galatsis K, Cukrov L, Włodarski W, McCormick P, Kalantar-zadeh K, Comini E, Sberveglieri G (2003) *Sens Actuators B* 93:562
- Ávila H, Rodríguez-Páez JE (2009) *J Non-Cryst Solids* 355:885
- Zhang Y, Tang J, Hu X (2008) *J Alloys Compd* 462:24
- Martinelli A, Ferretti M (2003) *Mater Res Bull* 38:1629
- Zuo J, Xu C, Liu X, Wang C, Wang C, Hu Y, Qian Y (1994) *J Appl Phys* 75(3):1835

33. Diéguez A, Romano-Rodríguez A, Morante J, Weimar U, Schweizer-Berberich M, Göpel W (1996) *Sens Actuators B* 31:1
34. Batzill M, Diebold U (2005) *Progr Surf Sci* 79:47
35. Lupan O, Chow L, Chaic G, Schulte A, Park S, Heinrich H (2009) *Mater Sci Eng B* 157:101
36. Owens F (2009) *J Mag Mag Mater* 321:2386
37. Grzeta B, Takalcec E, Goebbert C, Takeda M, Takahashi M, Nomura H, Jaksic M (2002) *J Phys Chem Solids* 63:765
38. Sanchez LC, Arboleda JD, Saragovi C, Zysler RD, Barrero CA (2007) *Physica B* 389:145
39. Sánchez LC, Beltrán JJ, Osorio J, Calle AM, Barrero CA (2010) *Hyperfine Interact* 195:185
40. Berry F, Greaves C, Helgason G, McManus J, Palmer H, Williams R (2000) *J Solid State Chem* 151:157